

#### Contents lists available at ScienceDirect

# **Photoacoustics**

journal homepage: www.elsevier.com/locate/pacs



#### Research article

# Simulations and human cadaver head studies to identify optimal acoustic receiver locations for minimally invasive photoacoustic-guided neurosurgery



Michelle T. Graham<sup>a,\*</sup>, Jiaqi Huang<sup>b</sup>, Francis X. Creighton<sup>c</sup>, Muyinatu A. Lediju Bell<sup>a,b,d</sup>

- <sup>a</sup> Department of Electrical and Computer Engineering, Johns Hopkins University
- <sup>b</sup> Department of Biomedical Engineering, Johns Hopkins University
- <sup>c</sup> Department of Otolaryngology Head and Neck Surgery, Johns Hopkins Medicine
- <sup>d</sup> Department of Computer Science, Johns Hopkins University

#### ARTICLE INFO

# Keywords: Photoacoustic imaging Ultrasound imaging Transcranial imaging Patient specific simulations Surgical guidance

#### ABSTRACT

Real-time intraoperative guidance during minimally invasive neurosurgical procedures (e.g., endonasal transsphenoidal surgery) is often limited to endoscopy and CT-guided image navigation, which can be suboptimal at locating underlying blood vessels and nerves. Accidental damage to these critical structures can have severe surgical complications, including patient blindness and death. Photoacoustic image guidance was previously proposed as a method to prevent accidental injury. While the proposed technique remains promising, the original light delivery and sound reception components of this technology require alterations to make the technique suitable for patient use. This paper presents simulation and experimental studies performed with both an intact human skull (which was cleaned from tissue attachments) and a complete human cadaver head (with contents and surrounding tissue intact) in order to investigate optimal locations for ultrasound probe placement during photoacoustic imaging and to test the feasibility of a modified light delivery design. Volumetric x-ray CT images of the human skull were used to create k-Wave simulations of acoustic wave propagation within this cranial environment. Photoacoustic imaging of the internal carotid artery (ICA) was performed with this same skull. Optical fibers emitting 750 nm light were inserted into the nasal cavity for ICA illumination. The ultrasound probe was placed on three optimal regions identified by simulations: (1) nasal cavity, (2) ocular region, and (3) 1 mm-thick temporal bone (which received 9.2%, 4.7%, and 3.8% of the initial photoacoustic pressure, respectively, in simulations). For these three probe locations, the contrast of the ICA in comparative experimental photoacoustic images was 27 dB, 19 dB, and 12 dB, respectively, with delay-and-sum (DAS) beamforming and laser pulse energies of 3 mJ, 5 mJ, and 4.2 mJ, respectively. Short-lag spatial coherence (SLSC) beamforming improved the contrast of these DAS images by up to 15 dB, enabled visualization of multiple cross-sectional ICA views in a single image, and enabled the use of lower laser energies. Combined simulation and experimental results with the emptied skull and > 1 mm-thick temporal bone indicated that the ocular and nasal regions were more optimal probe locations than the temporal ultrasound probe location. Results from both the same skull filled with ovine brains and eyes and the human cadaver head validate the ocular region as an optimal acoustic window for our current system setup, producing high-contrast (i.e., up to 35 dB) DAS and SLSC photoacoustic images within the laser safety limits of a novel, compact light delivery system design that is independent of surgical tools (i.e., a fiber bundle with 6.8 mm outer diameter, 2 mm-diameter optical aperture, and an air gap spacing between the sphenoid bone and fiber tips). These results are promising toward identifying, quantifying, and overcoming major system design barriers to proceed with future patient testing.

# 1. Introduction

Endoscopic transsphenoidal surgery is a minimally invasive technique frequently used to remove pituitary tumors and access the

anterior skull base [1–3]. Instruments are inserted through the nasal cavities to drill away the posterior face of the sphenoid sinus, gain access the skull base and dura of the cavernous sinus, and resect tumors [4,5]. This procedure is generally safe, with mortality rates of 0.2 -

E-mail addresses: mgraha33@jhu.edu (M.T. Graham), mledijubell@jhu.edu (M.A. Lediju Bell).

<sup>\*</sup> Corresponding author.

1.2% for experienced to novice surgeons [6]. Nonetheless, critical structures such as the internal carotid arteries (ICAs), optic nerves, and cranial nerves are within millimeters of the surgical site and are therefore susceptible to iatrogenic injury at a rate of 6.8% [7], which can have surgical complications including paralysis, visual loss, stroke, cerebral spinal fluid leaks, hemorrhage, and death [7], with morbidity and mortality rates as high as 14% and 24 - 40%, respectively, each time an accidental injury occurs [6,8,9]. In addition, over 50% of patients with residual disease or growth hormone-secreting tumors undergo re-operations [10], which increases the risk to individual patients experiencing this surgery more than once in their lifetimes. Revision surgeries also tend to have increased scarring, loss of natural anatomical markers, and disruption of ICA locations, which increase the risk of surgical complications from 6.8% to 11.4% in these cases [7].

Within the surgical site, the left and right ICAs are typically separated by 1.24 - 2.67 cm [11], which highlights the tight surgical workspace and motivates the need to closely monitor the location of the ICAs. While stereotactic guidance and endoscopy are primary monitoring techniques for endonasal transsphenoidal surgeries, these techniques suffer from two known limitations. First, stereotactic guidance is subject to registration errors which can become increasingly large as patient anatomy is disrupted during surgery and as the anatomy significantly deviates from that shown in preoperative x-ray computed tomography (CT) or magnetic resonance (MR) images. The second limitation is that endoscopy is unable to identify critical structures underlying bone or other tissues in the operative path [12]. An intraoperative imaging technique that provides real-time navigation of the complex, subsurface anatomy of the anterior skull would greatly assist surgeons with avoiding severe complications caused by these two well-known limitations.

Photoacoustic imaging has been demonstrated as a promising intraoperative imaging technique for neurological and neurosurgical [13–19] procedures. In photoacoustic imaging, optical energy incident on an optically absorbing target is converted into acoustic energy [20]. In transcranial photoacoustic imaging, a light delivery system inserted into the nasal cavity can cause photoacoustic excitation of naturally occurring chromophores, such as hemoglobin in blood vessels and lipids within the myelin sheath of nerves [21]. An externally placed ultrasound probe can receive the photoacoustic signals to create photoacoustic images.

Transcranial photoacoustic imaging is challenged by the reverberation, aberration, and attenuation of acoustic waves, which combine to degrade image quality. These adverse effects are primarily caused by the heterogeneity of cranial bone and the acoustic impedance mismatch between bone and cranial tissues [22–24]. Limited optical penetration through bone additionally complicates transcranial photoacoustic imaging [22,25–27]. Image processing techniques specific to transcranial photoacoustic imaging have been developed to improve target resolution, contrast, and localization in the presence of skull bone [28–30].

Previous work additionally explored imaging requirements specific to applying transcranial photoacoustic imaging as an endonasal intraoperative surgical navigation technique. In these studies, blood vessel mimicking targets composed of Tygon tubing and *ex vivo* bovine blood were imaged through varying thicknesses of cranial bone in plastisol and brain tissue phantoms [14–17]. These studies proposed the temporal region as the location of the ultrasound probe, considering that the temporal bone is generally accepted as the ideal acoustic window for transcranial ultrasound imaging [31]. In addition, Purkayastha *et al.* [31] investigated three potential ultrasound probe locations for transcranial imaging, including the transorbital, submandibular, and suboccipital windows. To the authors' knowledge, no similar comparative studies of external acoustic windows have been performed for transcranial photoacoustic imaging.

Considering the initially proposed temporal probe placement, minimum energy requirements for visualization of photoacoustic targets with delay-and-sum (DAS) beamforming were determined to be 1.2 - 5.9 mJ in the presence of 0 - 2 mm-thick temporal and sphenoid bones [16]. Short-lag spatial coherence (SLSC) imaging, an advanced beamforming technique previously shown to enhance target contrast when compared to DAS beamforming [32–34], was applied to transcranial photoacoustic imaging when penetrating thicker bone [14,17]. In addition, simultaneous visualization of a neurosurgery drill bit tip and phantom ICAs indicated that photoacoustic imaging has the potential to provide necessary spatial information to avoid ICA damage [16,35,36].

In this paper, we build on previous experimental setups by performing transcranial photoacoustic imaging with intact adult human skulls. These intact skulls provide insights into the relationships between complex bony skull anatomy and acoustic wave propagation challenges (e.g., sound reverberation and attenuation), and the effects of these challenges on photoacoustic image quality. In addition, we reassess previously defined bone thickness and contrast interrelationships and minimum energy requirements for ICA visualization in the presence of this complex skull anatomy. We also analyze the feasibility of temporal probe placement for transcranial photoacoustic imaging. Our reassessments and analyses include both amplitude-based (i.e., DAS) and coherence-based (i.e., SLSC) beamformers. An additional contribution of this paper is the first known comparative exploration of three acoustic windows for transcranial photoacoustic imaging (i.e., ocular, nasal, and temporal).

This paper is organized as follows. Section 2 describes our simulation and experimental methods, including the rationale and demonstration of a novel light delivery design for clinical translation. Section 3 presents our results, where simulations of an empty skull serve the three-fold purpose of identifying optimal external ultrasound probe locations (Section 3.1.1), explaining the acoustic sound trapping observed inside the skull (Section 3.1.2), and analyzing the localized acoustic pressure on the surface of the skull (Section 3.1.3). Simulations of a fresh cadaver head were additionally implemented to perform localized acoustic pressure analyses (Section 3.2). A comparative experimental study with the same empty skull that was simulated is then presented to confirm simulation results showing that the nasal cavity and ocular region are more feasible probe locations (Section 3.3.2) than the temple region (Section 3.3.1). Adding brain and eye tissue to the empty skull setup introduced additional acoustic material to confirm simulation results regarding the ocular probe location and to investigate light delivery design requirements for imaging the ICA targets within laser safety limits (Section 3.4). We then present results from a complete human cadaver head, which validate the ocular region as a feasible ultrasound probe location for clinical translation with our novel light delivery design (Section 3.5). In Section 4, we discuss probe location comparisons from the perspectives of image quality, image interpretability, and practical feasibility. We also discuss future opportunities and challenges for integrating optimal ultrasound probe locations into current practice. Section 5 summarizes our major conclusions.

## 2. Materials and Methods

#### 2.1. k-Wave Simulations

Three-dimensional photoacoustic simulations were performed using the k-Wave toolbox [37,38], based on CT volumes of two intact human cadaver specimens. The first specimen was an empty human skull that was cleaned from tissue attachments and provided by The Phantom Laboratory (Salem, NY). The second specimen was a fresh, formalinfixed cadaver head obtained from the Maryland Department of Health Anatomy Board. The CT volumes of these two specimens were converted into heterogeneous density and sound speed volumetric maps to generate the simulation medium. For the empty skull specimen, the skull surface was segmented from the CT volume and acoustic sensors

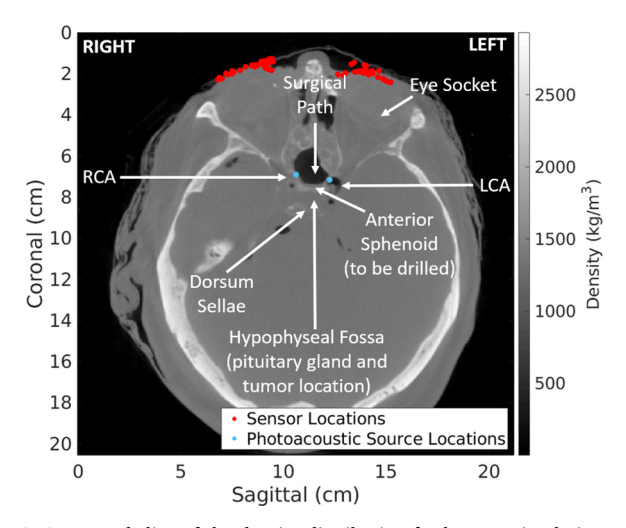


Fig. 1. Annotated slice of the density distribution for k-Wave simulations, derived from a corresponding axial CT slice of the fresh human cadaver head. Acoustic sensors were distributed across the eyelid surfaces as shown. The location of simulated photoacoustic sources for the LCA and RCA are also shown. Each source was simulated independently in the simulations based on this fresh cadaver head.

were distributed across the external skull surface. For the fresh cadaver head, CT images were acquired before the surgical procedure was performed, and acoustic sensors were distributed across the eyelid and eye surfaces of these preoperative images.

To illustrate the relationship between sensor and source locations and general anatomy of interest, Fig. 1 shows an axial slice of the simulated density distribution derived from the CT of the fresh cadaver head and annotated with anatomical landmarks, acoustic sensor locations, and photoacoustic source locations. The right and left ICAs are approximately 4 mm in diameter and reside on either side of the sella turcica, a bony saddle-like structure composed of the anterior sphenoid, the hypophyseal fossa (i.e., the depression where the pituitary gland rests), and the dorsum sellae (i.e., the bony wall dividing the sella turcica from the cranial cavity).

For each specimen simulation, photoacoustic sources were placed within the left and right ICAs. We assumed an equivalent fluence incident on each ICA, resulting in an initial pressure amplitude of 403 Pa for each source. The signal energy received by each sensor location was calculated as:

$$E_{s} = \sum_{t=0}^{N} |x(t)|^{2} \tag{1}$$

where x(t) is the time domain pressure signal and N is the total simulation time in seconds. The Courant-Friedrichs-Lewy numbers (which influence simulation accuracy and overall simulation times [38,39]) were 0.15 and 0.10 for the empty skull and cadaver head specimens, respectively. No shear waves were included in these simulations.

## 2.2. Photoacoustic Imaging System

The photoacoustic imaging system used for experimental studies consisted of a Phocus Mobile laser (Opotek, Carlsbad, CA, USA) and E-Cube 12R ultrasound scanner connected to an SP1-5 phased array ultrasound probe (Alpinion Medical Systems, Seoul, South Korea). The OPO of the laser was tuned to a fixed wavelength of 750 nm in order to excite deoxyhemoglobin (which we assume to be the endogenous chromophore in our experimental blood). Fig. 2 shows that there are multiple wavelength options to excite oxyhemoglobin in the ICAs during surgery, which has an optical absorption spectra that is orders of magnitude greater than that of other tissues surrounding the surgical site (e.g., bone, brain matter, collagen, lipids, and water [40–45]). At

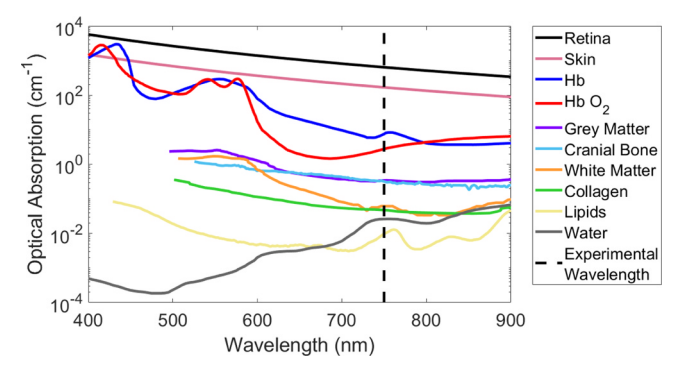


Fig. 2. Optical absorption spectra of endogenous biological chromophores [40–47]. A wavelength of 750 nm was chosen to excite our experimental blood.

our chosen wavelength of 750 nm, the American National Standards Institute (ANSI) only defines the maximum permissible exposure (MPE) for two biological organs (i.e., human skin and retinal tissue). Considering the orders of magnitude higher optical absorption of retina and skin compared to other tissues within the surgical site, as shown in Fig. 2, the established safety limits are likely conservative for other biological tissues [40-48]. Nonetheless, we chose to benchmark our methods against the MPE for skin, which is 25.2 mJ/cm<sup>2</sup> for 750 nm light [49]. Table 1 summarizes the maximum allowable energy using this MPE for the four light delivery methods that were individually coupled to the OPO output of the laser. These light delivery methods were compared and tested in order to investigate three system design components: (1) energy requirements, (2) ability to image within safety limits, and (3) ability to meet these energy and safety requirements while maintaining a sufficiently small form factor to operate within the nasal cavity.

Three of the light delivery methods were commercially available, including a 5 mm-core-diameter fiber bundle, a 1 mm-core-diameter optical fiber, and a 2 mm-core-diameter fiber bundle, as shown in Figs. 3(a,c), 3(b), and 3(d), respectively. The fourth light delivery method was the 2 mm-core-diameter fiber bundle, with its terminal end modified for insertion into a 1.67 cm length, 4 mm-inner-diameter, and 6 mm-outer-diameter hollow quartz tube as shown in Fig. 4(b) (more details about the rationale for this fourth design appear in Section 3.4).

# 2.3. Intact Human Skull Experiments

## 2.3.1. Pre-experiment Specimen Preparations

Experiments were performed with the intact human skull shown in Fig. 3 and used for the simulations described in Section 2.1. The anterior sphenoid bone was removed to expose the skull base (as is typical in transsphenoidal procedures). Phantom ICAs were created by fixing 4 mm-inner-diameter Tygon tubing inside the skull in the correct anatomical location on either side of the sella turcica.

The phantom ICAs were injected with either India ink solution or whole human blood. India ink mixed with water was previously demonstrated to mimic the optical absorption of blood in the concentration range 0.03 - 0.13% [50,51]. We repeated similar experiments to determine the concentration that matched the contrast of photoacoustic signals originating from the whole human blood of Johns Hopkins Hospital patients (with approval from the Institutional Review Board), and determined that 0.5% India ink solution provided the best match. Therefore, to perform the experiments described in Sections 2.3.2 and 2.3.3, a solution of 0.5% India ink and water was injected into the phantom ICAs. To perform the experiments in Section 2.3.4, the phantom ICAs were injected with whole human blood from Johns Hopkins Hospital patients.

For each experiment described in Sections 2.3.2 - 2.3.4, the prepared skull was fixed in a Mayfield clamp and submerged in a water bath for acoustic coupling. The skull was degassed for 30 minutes after

Table 1
Summary of light delivery design parameters and corresponding maximum allowable output laser energy at the tip of each light delivery method, using a 25.2 mJ/cm² safety limit for 750 nm wavelength light. The maximum allowable energy reported for the 2 mm-core-diameter fiber bundle with quartz spacer was calculated using the area shown in Fig. 4(c).

Light Delivery Method	Outer Diameter (mm)	Numerical Aperture	Maximum Allowable Energy (mJ)
5 mm-core-diameter fiber bundle	15	0.22	4.95
1 mm-core-diameter fiber bundle	6.1	0.50	0.20
2 mm-core-diameter fiber bundle	6.8	0.22	0.80
2 mm-core-diameter fiber bundle with quartz spacer	6.8	0.22	9.32

submersion and prior to imaging. In addition, the chosen light delivery method was inserted into the nasal cavity to illuminate the phantom ICAs.

#### 2.3.2. Temporal Bone Feasibility Study

Building on the previous work of Bell *et al.* [16], which demonstrates an experimental phantom study to image blood through 0 - 2.5 mm-thick temporal bone fragments in the presence of ovine brain tissue, we performed a similar study with the intact human skull. The purpose of our study was to reassess energy requirements for transcranial photoacoustic imaging of phantom ICAs in this more complex acoustic environment.

In addition to the anterior sphenoid bone removed from the intact skull, a 2 cm x 3 cm region of the temporal bone was removed from this skull via a middle fossa craniotomy to create a variable thickness temporal bone window. This variable thickness window was created by covering the area of the removed bone window with one of five approximately 3 cm x 3.3 cm human cadaver skull bone fragments, as shown in Fig. 3(a). The skull fragments were cut from formalin-fixed temporal bone specimens, manually cleaned from tissue attachments,

and sanded to a desired thicknesses. The thickness of each fragment measured 0 mm (no fragment present), 1.0 mm, 1.3 mm, 3.0 mm, or 4.4 mm. For each thickness, the ultrasound probe was fixed in the same location, as shown in Fig. 3(a), to control the thickness of the transcranial acoustic pathway for this systematic study.

The 5 mm-core-diameter fiber bundle was inserted in the nasal cavity, as shown in Fig. 3(a). The following pulse energies were emitted from the tip of the fiber bundle for each temporal bone thickness: 0.08, 0.28, 4.20, 11.0, 21.0, 34.0, 47.0, 61.0, and 75.0 mJ. For this study, results are reported as functions of the five temporal bone thicknesses and these nine laser energies.

## 2.3.3. Probe Location Comparison

To experimentally confirm results from the k-Wave simulations described in Section 2.1, the ultrasound probe was placed on two additional regions of the intact skull: (1) the nasal cavity and (2) the ocular region, as shown in Figs. 3(b) and 3(c), respectively. These two additional probe locations were investigated prior to drilling away the temporal bone for the study described in Section 2.3.2. Due to space constraints, the 1 mm-core-diameter fiber was utilized to image through

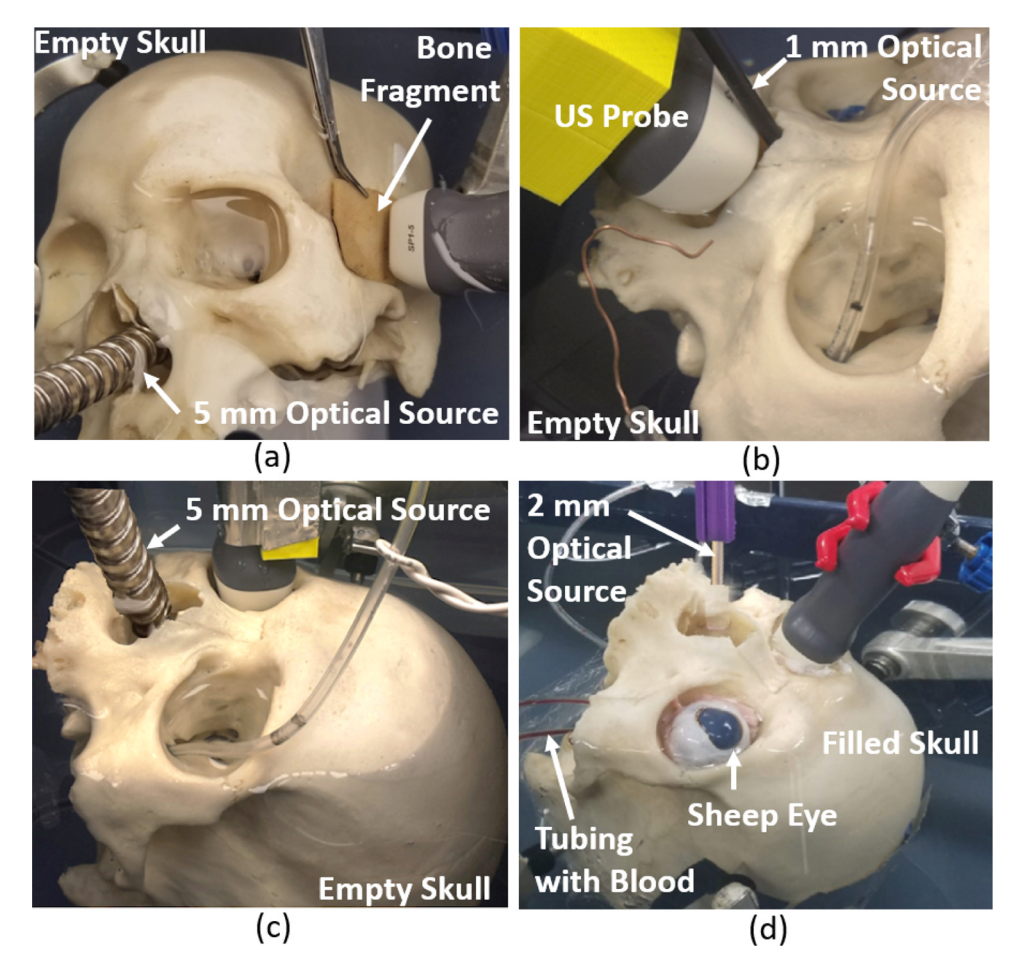


Fig. 3. Experimental setups for the intact skull, cleaned from tissue attachments. (a) Empty skull with the 5 mm-core-diameter fiber bundle as the optical source and the ultrasound probe placed on the 1 mm-thick temporal bone fragment. (b) Empty skull with the 1 mm-corediameter optical fiber as the optical source and the ultrasound probe placed on the nasal cavity. (c) Empty skull with the 5 mm-corediameter fiber bundle as the optical source and the ultrasound probe placed on the right ocular region. (d) Skull filled with brain tissue and eye sockets filled with ovine eyes with the 2 mm-core-diameter fiber bundle as the optical source and the ultrasound probe placed on the right ovine eye. The Tygon tubing was filled with whole human blood for this experiment.

the nasal cavity, with an energy limited to 3 mJ per pulse at the fiber tip. Otherwise, the 5 mm-core-diameter fiber bundle was utilized, and it emitted 5 mJ per pulse for the ocular probe location. The results from these ocular and nasal probe placements were compared to results obtained from the study described in Section 2.3.2 with the 1 mm-thick temporal bone window and 4.2 mJ laser energy.

## 2.3.4. Ocular Imaging Experiments with Filled Skull

To assess the combined impact of tissue attenuation, space constraints, and fluence limits on photoacoustic image quality and their relationship to light delivery design requirements, ovine brain tissue was placed to fill the frontal cranium, ovine eyes were placed in the ocular region, and whole human blood was injected into the phantom ICAs, as shown in Fig. 3(d). The drilled away anterior sphenoid bone was used as a variable thickness sphenoid window by covering the area with one of five total 1.5 cm diameter circular human cadaver skull bone fragments which were prepared using the same methods as the fragments described in Section 2.3.2. The thickness of each fragment was 0 mm (no fragment present), 0.5 mm, 1.3 mm, 2.1 mm, or 3.3 mm.

The light delivery system was downsized from the 5 mm-core-diameter (15 mm-outer-diameter) fiber bundle to the 2 mm-core-diameter (6.8 mm-outer-diameter) fiber bundle to enable navigation in the average adult nasal cavity for this experiment. In order to explore the feasibility of obtaining suitable images while maintaining laser safety limits with this smaller light delivery system, the laser spot size incident on the tissue was increased by increasing the distance between the laser tip and sphenoid bone surface. For repeatable laser tip placement, this fiber bundle was affixed to the end effector of a UR5e robot arm (Universal Robots Company, Odense, Denmark). After touching the sphenoid bone, the laser tip was retracted, pausing at the five waypoints listed in Table 2. This table cross-references waypoint locations, their associated spot sizes incident on the sphenoid bone (calculated using geometrical optical principles), and maximum allowable energy output per pulse. At each waypoint and each sphenoid bone thickness, the RCA was imaged with the following pulse energies: 0.10 mJ, 0.90 mJ, 1.30 mJ, 2.20 mJ, 5.40 mJ, 7.50 mJ, 10.6 mJ and 13.8 mJ. For this experiment, results are reported as functions of sphenoid bone thickness, waypoint positions, and the eight laser energies.

Table 2
Summary of the five waypoints investigated during the skull experiment with brain tissue, including x-z coordinates with respect to sphenoid bone surface, Euclidean distance between each waypoint and the sphenoid bone surface, calculated laser spot diameter incident on sphenoid surface (based on geometrical optical principles), and the resulting maximum allowable energy.

La	aser Tip Location		Waypoint	Laser Tip to Sphenoid Bone Distance	Laser Spot Diameter (cm)	Maximum Allowable Energy (mJ)
35			Е	3.05 cm	1.02	25.57
30		• E				
25			D	2.08 cm	0.55	13.93
Ē 20	• D					
20 axis (mm) six z 215	• C		C	1.64 cm	0.39	9.80
10	• B					
5	- 5		В	0.89 cm	0.18	4.43
0 A	2 x axis (mm)	4	A	0.00 mm	0.03	0.80

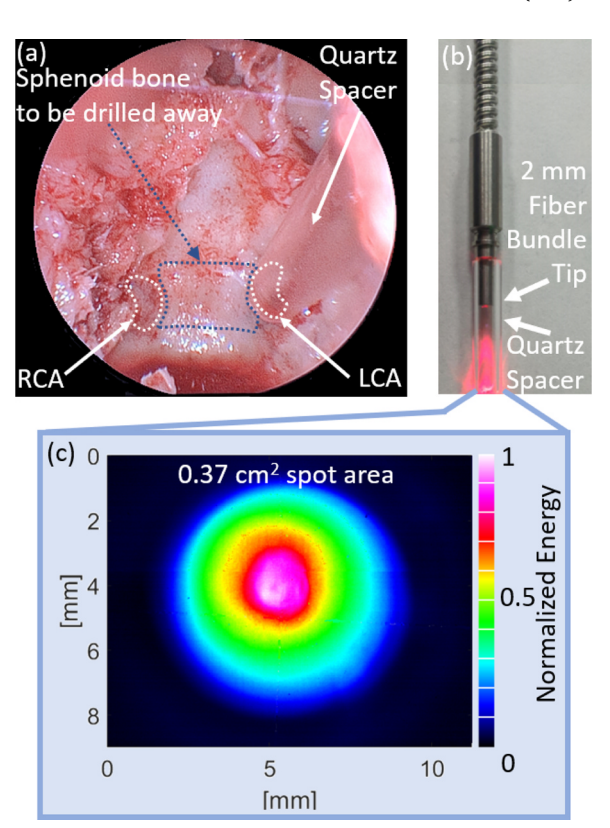


**Fig. 4.** (a) Endoscopic image of the sphenoid sinus of the fresh cadaver head. The left and right carotid arteries (LCA and RCA, respectively) are located on either side of the sphenoid bone to be removed. The quartz spacer attached to the terminal end of the fiber bundle is visualized in the endoscopic field of view and is directed to illuminate the RCA. (b) Photograph of the 2 mm-core-diameter fiber bundle with quartz spacer, emitting 690 nm light (for visualization only). (c) Expected beam profile incident on the sphenoid surface when emitting 750 nm light during the fresh cadaver head experiments.

# 2.4. Fresh Cadaver Head Studies

Experiments with a complete human cadaver head were performed to test the translatability of results from the experiments described in Sections 2.1 - 2.3. After obtaining CT images and noticing air cavities in the ICAs of this cadaver head (e.g., see Fig. 1), an additional 10 - 14 mL of whole human blood was injected in each ICA, superior to the common carotid. These carotid arteries in the neck were sutured after this injection. An endonasal surgery was performed on this fresh human cadaver head in order to expose the anterior face of the sphenoid bone.

After fixing the cadaver head in a Mayfield clamp, a 3 mm diameter, 30 degree nasal endoscope (Karl Storz, Tuttlingen, Germany) was inserted into the sphenoid sinus to produce the image shown in Fig. 4(a). This image is annotated to highlight sphenoid bone that would be removed in a surgical procedure to access the skull base. Similarly, the white bounded areas highlight the visually determined locations of the LCA and RCA, which have an intracarotid distance of 1.5 cm and are covered by 0.8 - 1.4 mm-thick and 1.1 - 2 mm-thick bone, respectively, as measured in the preoperative CT images. These ICAs were visually identified using anatomical landmarks and the subtle color visible through the thin bone covering these ICAs.

The 2 mm-core-diameter fiber bundle terminated with the quartz tube (mentioned in Section 2.2 and shown in Fig. 4(b)) was inserted through the nasal cavity, stopping at the anterior face of the sphenoid bone in the sphenoid sinus, as shown in Fig. 4(a). Without the quartz spacer, this fiber bundle is limited to a maximum energy of 0.80 mJ per pulse at the fiber tip in order to operate within safety limits, as indicated in Table 1. However, the results in Section 3.4 describe that 2.2

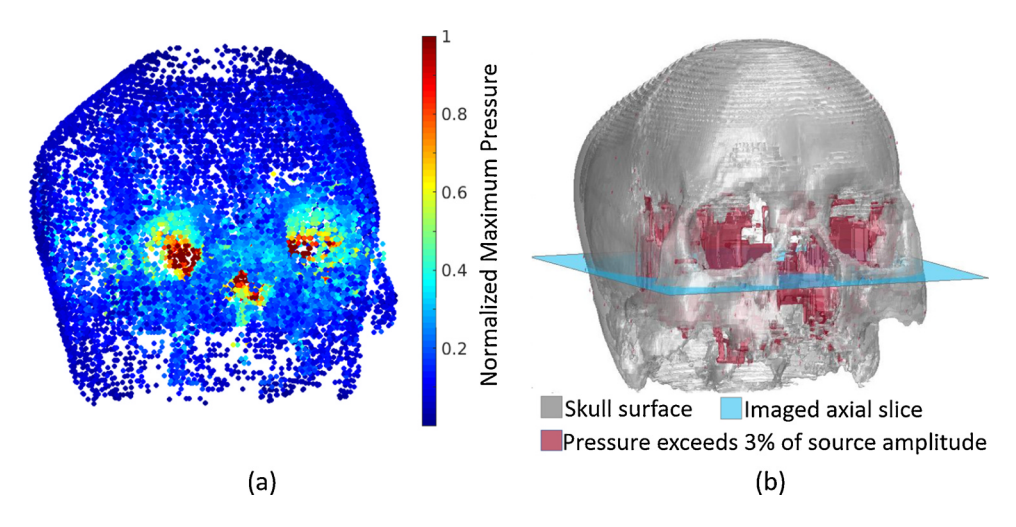


Fig. 5. (a) k-Wave simulation results from acoustic sensors distributed across the external surface of the empty skull, showing the maximum pressure received by each sensor (over the entire simulation duration). (b) Summary of the maximum pressure received by each sensor exceeding 3% of the initial source pressure, mapped as red-shaded surfaces on the 3D CT reconstruction. The axial plane intersecting the nasal cavity corresponds to the image plane of Fig. 6.

mJ per pulse is the minimum energy for ICA visualization with the ocular probe position. Therefore, the quartz spacer was added to increase the incident 1/e spot area to  $0.37~cm^2$  at the spacer tip, as shown in Fig. 4(c). This spot size was measured with a beam profiler (Edmund Optics, Barrington, New Jersey, USA) and allows a maximum operable energy of 9.32~mJ per pulse to satisfy laser safety limits. Therefore, the threefold purpose of the spacer is to provide a physical barrier to ensure that the desired distance is maintained, decrease the likelihood of exceeding safety limits, and relieve the operator from the burden of manually maintaining a minimum spot size without the spacer, which overall improves device safety and usability.

The fiber bundle was positioned to independently illuminate the left and right ICAs, as shown in Fig. 4(a) for the RCA. The laser energy was varied from 0.9 to 13.1 mJ. The ultrasound probe was placed on either the left or right closed eyelid of the human cadaver head.

# 2.5. Validation with CT Registration

The signals in the photoacoustic images obtained during the experiments described in Sections 2.3 - 2.4 were validated using CT registration. Ultrasound images were acquired for anatomical reference after each photoacoustic image acquisition. The CT slices corresponding to the ultrasound imaging planes in the empty skull, filled skull, and fresh head experiments were manually extracted from the CT volume based on an estimate of the ultrasound probe imaging plane used in each experiment. Anatomical features in ultrasound images were then used to perform landmark registration between ultrasound images and CT slices using 3D Slicer [52]. This ultrasound-to-CT image registration was sufficient to produce the final photoacoustic-to-CT image registration, because photoacoustic imaging utilizes the same acoustic receiver and therefore, the resulting photoacoustic images are inherently co-registered to the ultrasound images.

## 2.6. Image Quality Metrics

Photoacoustic images were reconstructed with DAS and SLSC beamformers. Photoacoustic DAS and SLSC image contrast was measured for experimental images, defined as follows:

$$Contrast = 20\log_{10}\left(\frac{\mu_t}{\mu_b}\right) \tag{2}$$

where  $\mu_t$  and  $\mu_b$  are the mean values within rectangular regions of interest (ROIs) corresponding to the photoacoustic signal and background regions of the beamformed data. The signal ROI was centered on the brightest pixel in the photoacoustic image. The rectangular ROI size was chosen to encompass the photoacoustic signal (i.e., approximately 2 mm x 0.7 mm). Each background ROI was the same size as the signal

ROI and laterally shifted by 21 - 29 mm from the signal ROI. Visual inspection confirmed that the background ROIs primarily contained background signals representative of the electronic noise of the system. When analyzing photoacoustic image contrast as a function of pulse energy, ROIs were selected once for each bone thickness, using the photoacoustic image acquired with the highest pulse energy. This selection was then maintained for the remaining pulse energies.

Each photoacoustic image was normalized by the brightest pixel and displayed with 10 dB dynamic range. The short-lag value *M*, which is described in more detail in previous papers[32,53], was fixed at 15 for the SLSC images (i.e., 23% of the receive aperture). A minimum target contrast of 5 dB for DAS beamformed images was determined to be the threshold for ICA visualization in each DAS beamformed image. Similarly, contrast thresholds of 10 dB and 5 dB were visually determined from SLSC images of the intact human skull and fresh cadaver head, respectively. Plots of contrast as a function of energy for each temporal or sphenoid bone thickness were used to determine the minimum energy required for visibility by selecting the minimum tested pulse energy at which contrast exceeded the threshold in each plot.

## 3. Results

# 3.1. k-Wave Simulations of Empty Skull

## 3.1.1. Identification of Potential Ultrasound Probe Locations

Fig. 5(a) shows the maximum pressure received by each acoustic sensor distributed across the empty skull surface at the completion of the simulation. Fig. 5(b) summarizes this result by showing the locations of sensors that received a maximum pressure signal greater than or equal to 3% of the initial source pressure. The regions on the skull surface which met this pressure threshold were the nasal, ocular, and temple regions, which received 9.2%, 4.7%, and 3.8% of the initial photoacoustic pressure, respectively. These regions were identified as potential ultrasound probe locations.

#### 3.1.2. Acoustic Signal Trapping Due to Skull Anatomy

Fig. 6 demonstrates how the complex bony anatomy of the empty skull affects the propagation of acoustic waves. At time  $t_0$ , the axial slice through the simulation medium shows the circular cross-sections of the two initial pressure distributions located at the position of the ICAs. At time  $t_1$ , the pressure from the LCA and RCA propagated spherically outward from the initial location, and an acoustic reflection from the right anterior sphenoid region of the sella turcica is also observed. At time  $t_2$ , multiple acoustic reflections are observed, primarily originating from the anterior sphenoid bone and dorsa sellae, which reflect the acoustic signal back into the hypophyseal fossa. The reflected waves from the rounded edges of the dorsa sellae were observed to be

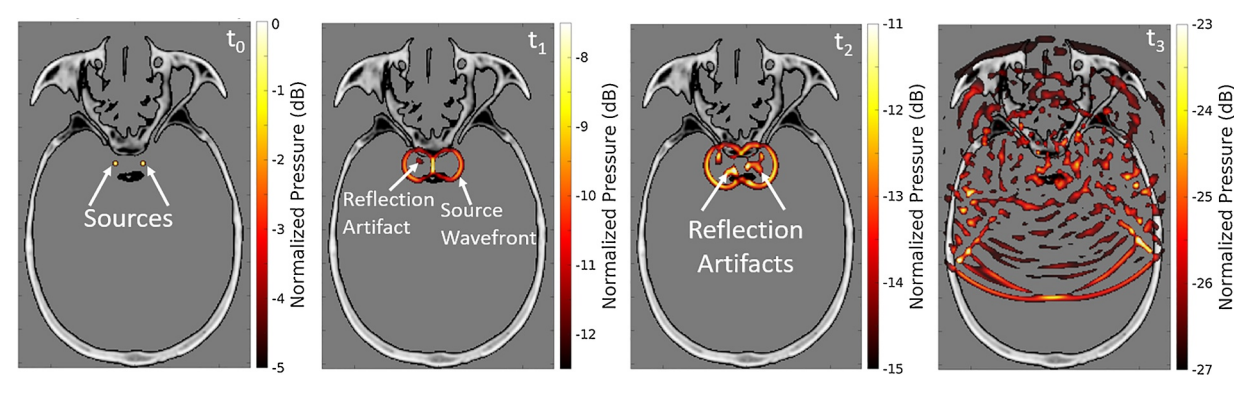


**Fig. 6.** Axial slices from 3D k-Wave simulations demonstrating acoustic wave propagation within the complex bony anatomy of the empty skull overlaid on the simulated density map, spanning times  $t_0$  to  $t_3$ . Time  $t_0$  shows the initial pressure distribution of the carotid sources. Time  $t_3$  shows the photoacoustic signals after traveling to the temporal bone. The photoacoustic signals in each image are normalized by the maximum photoacoustic amplitude at time  $t_0$ .

spherically propagating as if the reflective surface were another photoacoustic source, which is an expected source of artifacts in photoacoustic images. In addition, these reflections trap acoustic signal in the sella turcica, and the acoustic signal attenuates as it reverberates within the sella turcica. At time  $t_3$ , photoacoustic signals have traveled to the external skull surfaces, while acoustic signal also remains near the initial pressure distribution positions and within the sella turcica, and reverberations are observed throughout the cranial cavity.

#### 3.1.3. Localized Acoustic Pressure Analysis

Fig. 7 shows pressure signals received by a single acoustic sensor positioned in the nasal cavity, on the left and right ocular regions, and on the left and right temples of the empty skull. Sensors receiving the maximum pressure were chosen for each of these examples. The maximum received pressure of the sensor in the nasal cavity exceeds that of either the ocular (Fig. 7(a)) or temple (Fig. 7(b)) region by 16 Pa and 22 Pa, respectively. In addition, Fig. 7(a) shows that the sensors on the right and left eyes receive equivalent maximum pressures of 13 Pa. Fig. 7(b) shows that the sensors on the left temple received a maximum pressure that was 0.6 Pa greater than those on the right temple. Thus, there is minimal to no left-right asymmetry in these acoustic pathways (i.e., between the source and temple or between the source and ocular regions), making the left and right side equally preferable ultrasound probe locations for the simulated anatomy. Note that the maximum pressure received by these five sensor locations indicate a pressure decrease as the source-to-sensor distance increased, which is expected.

## 3.2. k-Wave Simulations of Fresh Cadaver Head

Fig. 8 shows the distribution of photoacoustic signal energy received by acoustic sensors located on the left and right eyes in the 3D k-Wave simulation of the fresh cadaver head, with signal energy calculated

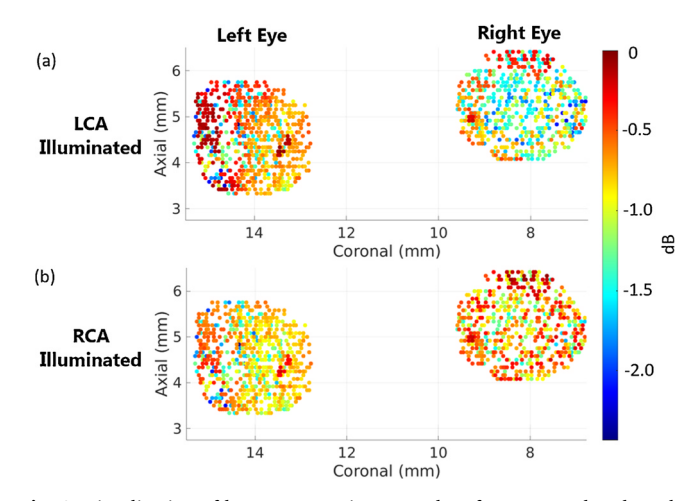


**Fig. 8.** Visualization of k-Wave acoustic sensor data for sensors placed on the left and right eyelids of the fresh cadaver head when the photoacoustic source is (a) the LCA and (b) the RCA. The colors indicate the total signal energy received by each sensor at the completion of each simulation, normalized by the maximum of the total signal energy for each simulation.

using Eq. (1). When the LCA was illuminated (Fig. 8(a)), the average signal energy received by all sensors located on the left and right eyes were  $12.8 \times 10^3 \ \text{Pa}^2$  and  $9.2 \times 10^3 \ \text{Pa}^2$ , respectively. When the RCA was illuminated (Fig. 8(b)), the average signal energy received by all sensors located on the left and right eyes were  $9.6 \times 10^3 \ \text{Pa}^2$  and  $12.4 \times 10^3 \ \text{Pa}^2$ , respectively.

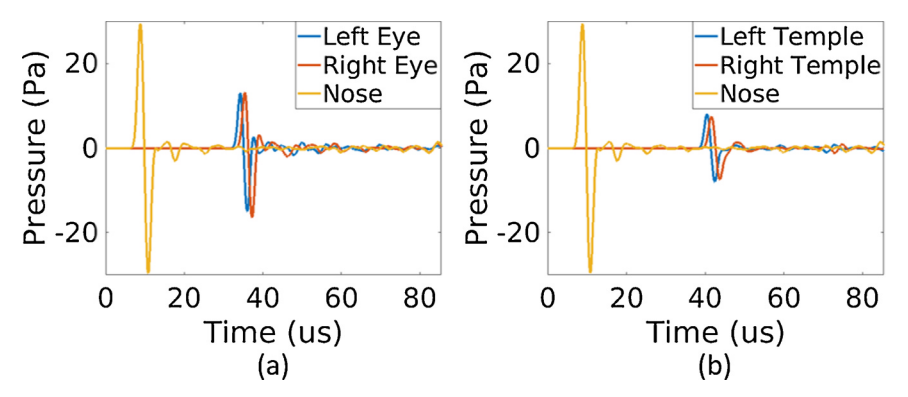


Fig. 7. Photoacoustic pressure signals from k-Wave simulations of the empty skull, each measured from a single sensor location (a) within the nasal cavity and ocular regions and (b) within the nasal cavity and temporal regions. The nasal sensor locations were identical for each plot and replicated to simplify comparisons.

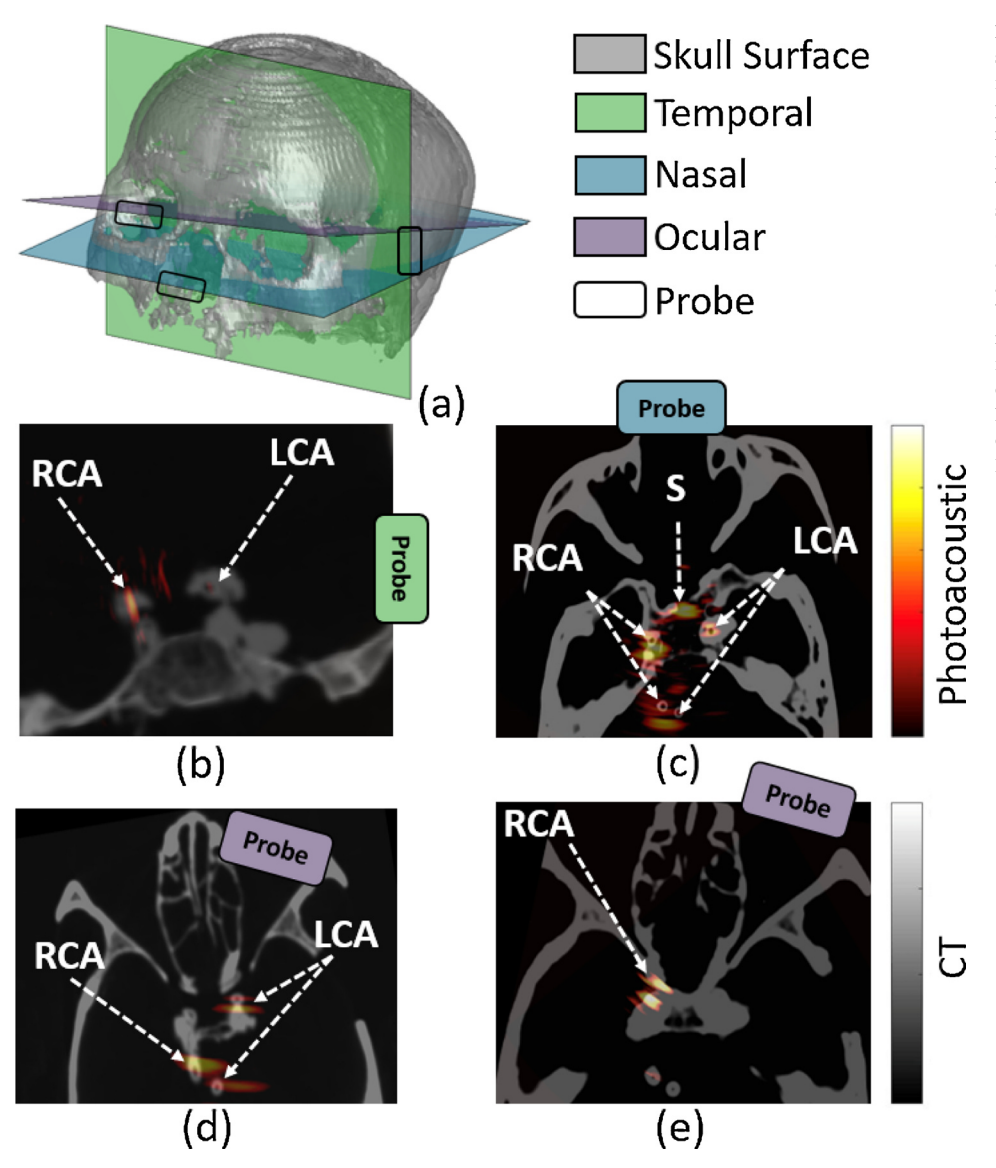


Fig. 9. (a) 3D CT reconstruction of the empty skull highlighting the axial-lateral ultrasound imaging planes and lateral-elevation ultrasound probe locations used for the temporal region. nasal cavity, and ocular regions. Co-registered photoacoustic and CT images of the empty skull with the axial-lateral dimension of the ultrasound probe placed on the (b) temporal region (with no temple bone), (c) nasal cavity region, and (d) ocular region. (e) Co-registered photoacoustic and CT images of the skull filled with brain tissue and ultrasound probe placed on the right ocular region. The CT images are displayed in grayscale, and the photoacoustic images are displayed in color with 20 dB dynamic range. Photoacoustic targets include the LCA, RCA, and optical source (S). The Tygon tubing phantom ICAs appear as hollow circles on CT images.

#### 3.3. Empty Skull Experimental Results

#### 3.3.1. Temporal Probe Location is Not Optimal

Fig. 9(a) shows a 3D CT reconstruction of the empty skull, axiallateral ultrasound imaging planes, and lateral-elevation ultrasound probe locations used for the temporal region, nasal cavity, and ocular regions. A corresponding photoacoustic-to-CT image registration when the ultrasound probe was placed on the temple region is shown in Fig. 9(b). This registration shows that the photoacoustic signals originate from the same locations as the ICAs which confirms visualization of the ICA targets. When compared to Bell et al.'s previous study [16] with 1 mm temporal bone fragments, the reported target contrast ranged 9.0 - 19.2 dB when the laser operated with 2.0 - 9.3 mJ per pulse. Our new experimental results with the empty skull and 1 mm temporal bone resulted in ICA target contrast ranging 7.8 - 14.3 dB when the laser operated with 4.2 - 11.0 mJ per pulse. Although there is an overlap of contrast values reported for the two experiments, our newer experiment generally reports lower contrast values, which motivates additional investigation of the temporal region as a probe location using the intact skull, as presented in Fig. 10.

Fig. 10(a) shows ICA target contrast in DAS images from the empty skull experiment as a function of energy for temporal bone thicknesses ranging 0 - 4.4 mm. The ICA target contrast increased as laser energy

increased and as temporal bone thickness decreased. For the range of energies tested, the ICA target contrast was consistently less than the empirically determined 5 dB visualization threshold when the temporal bone thickness was greater than 1.3 mm. Fig. 10(b) shows the corresponding minimum required energy to visualize the ICA targets in the presence of temporal bone, using the visually determined contrast threshold defined in Section 2.6. The dashed line in Fig. 10(b) shows the 4.95 mJ maximum allowable energy for the 5 mm-core-diameter fiber bundle (as reported in Table 1). The ICA targets were visualized in DAS and SLSC images within this safety limit when the temporal bone was < 1.3 mm and  $\leq$ 1.3 mm thick, respectively. However, the temporal bone of the human skull measures 1 - 4.4 mm thick [54]. Therefore, the temporal bone is considered as a less ideal ultrasound receiver location for photoacoustic imaging of the ICAs.

# 3.3.2. Probe Location Comparison

Figs. 9(c) and 9(d) show the location of the ICA targets visualized when the ultrasound probe was placed in the nasal and ocular regions, respectively. The corresponding photoacoustic DAS and SLSC images overlaid on ultrasound images from the nasal and ocular probe locations are shown in Figs. 11(b) and 11(c), respectively. Similarly, Fig. 11(a) shows co-registered ultrasound and photoacoustic images that correspond to the temporal probe location shown in Fig. 9(b). In

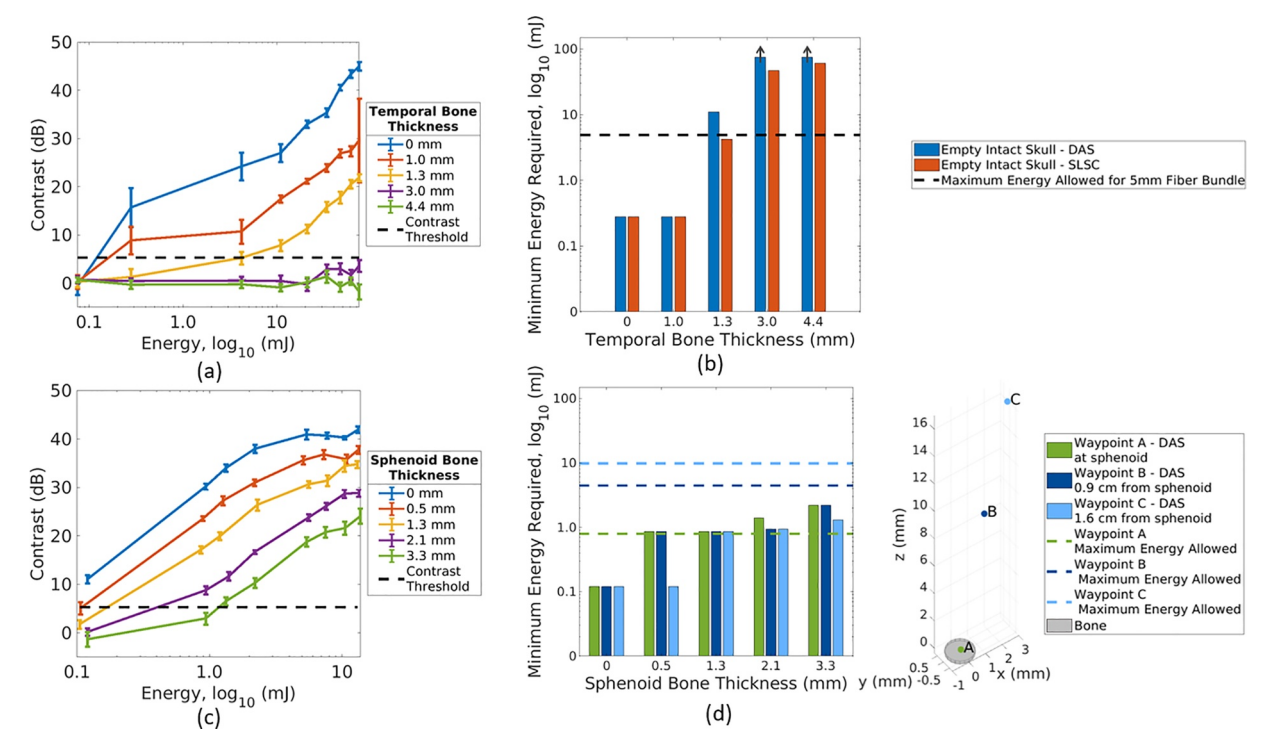


Fig. 10. Empty skull experiments: (a) RCA contrast in DAS images with temporal bone thicknesses ranging 0 - 4.4 mm, and pulse energies ranging 0.08 - 75.0 mJ (displayed on a log scale). (b) Minimum energy required to visualize the RCA in DAS and SLSC images when the probe was placed on temple region. The dashed line represents the 4.95 mJ maximum allowable energy for the 5 mm-core-diameter fiber bundle, as reported in Table 1. Arrows (†) represent minimum required energies which exceeded the maximum capable pulse energy of the optical source. Filled skull experiments: (c) RCA contrast in DAS images when the laser tip was located at waypoint C (1.64 cm away from sphenoid) for sphenoid bone thicknesses ranging 0 - 3.3 mm. Pulse energies ranged 0.10 - 13.8 mJ and are displayed on a log scale. (d) Minimum energy required to visualize the RCA in DAS images at waypoints A, B, and C when the probe was placed on the ocular region with sphenoid bone thicknesses ranging 0 - 3.3 mm. The dashed lines represent the maximum allowable energy calculated for the 2 mm-core-diameter fiber bundle without the quartz spacer attached, as reported in Table 2. A 3D visualization of waypoints A, B, and C with respect to the sphenoid bone surface is shown for reference.

particular, Fig. 11(a) demonstrates that the LCA, RCA, and optical source was visualized when imaging through the nasal cavity. The RCA in Fig. 11(a) was additionally observed to cross the imaging plane in two locations with SLSC imaging, while the DAS image created from the same data shows only the portion of RCA that is closest to the light source.

The presence of bony anatomical landmarks to assist with registration is another detail to consider. Specifically, the co-registered ultrasound image obtained with the nasal probe location provides useful bony anatomical features, as observed in Fig. 11(a). The photoacoustic DAS and SLSC images in Fig. 11(b) show that both the LCA and RCA were visualized with the ocular probe position along with a bony anatomical reference, although the light source was not seen. When imaging through 1 mm of bone on the right temple, only the RCA was visualized in the photoacoustic DAS and SLSC images, as shown in Fig. 11(c). In addition, these images provide no bony anatomical references (unlike the nasal and ocular images), and the temporal bone window cut-out was instead used as a landmark for registration in these cases.

The bottom of Fig. 11 presents quantitative contrast measurements for comparison. Because the photoacoustic signal from the RCA was consistently present in the three tested ultrasound probe positions, this signal was used for the quantitative comparison of photoacoustic image quality. The measured contrasts of the RCA in DAS photoacoustic images were 27 dB, 19 dB, and 12 dB for nasal, ocular and temporal regions, respectively. The corresponding contrasts in SLSC images were 41 dB, 35 dB, and 21 dB, respectively, resulting in a 9 - 16 dB improvement over DAS.

## 3.4. Filled Skull Results and Spacer Design Requirements

Similar to Figs. 9(b)-(d), Fig 9 (e) validates visualization of the RCA targets when brain tissue was present in the skull. For this setup, Fig. 10(c) shows RCA photoacoustic image contrast for one of the source-to-sphenoid distances (i.e., waypoint C). RCA contrast generally increased with increasing laser energy and decreased with increasing sphenoid bone thickness. Fig. 10(d) shows the minimum energy required to visualize ICA targets with 5 dB contrast for waypoints A, B, and C. For waypoint A, the minimum energy was equivalent to or exceeded the maximum allowable energy with 0.5 mm or thicker sphenoid bone. For waypoints B and C, the minimum energies for the thickest sphenoid bone (i.e., 1.3 - 2.2 mJ at 3.3 mm thickness) were lower than the maximum allowable energies of 4.43 and 9.80 mJ per pulse, respectively. Therefore, the 2 mm-core-diameter fiber bundle must be positioned at least 0.89 cm (i.e., the distance of waypoint B from the bone surface) from the surface of the surgical workspace in order to visualize the ICAs within safety limits. The larger distances we tested (i.e., waypoints D and E) may also be used to increase the maximum allowed energy and improve image quality. These results motivated the quartz spacer design for the fresh cadaver head results presented in Section 3.5.

# 3.5. Fresh Cadaver Head Results

Fig. 12 shows photoacoustic images from the ocular probe position overlaid on co-registered ultrasound or CT images of the fresh cadaver head. When imaging from the left eye, a significant level of background noise was present in the DAS image, which reduces the overall LCA contrast (Fig. 12(a)). Conversely, in the SLSC image, the background noise was significantly reduced, and the LCA was visualized with 30 dB

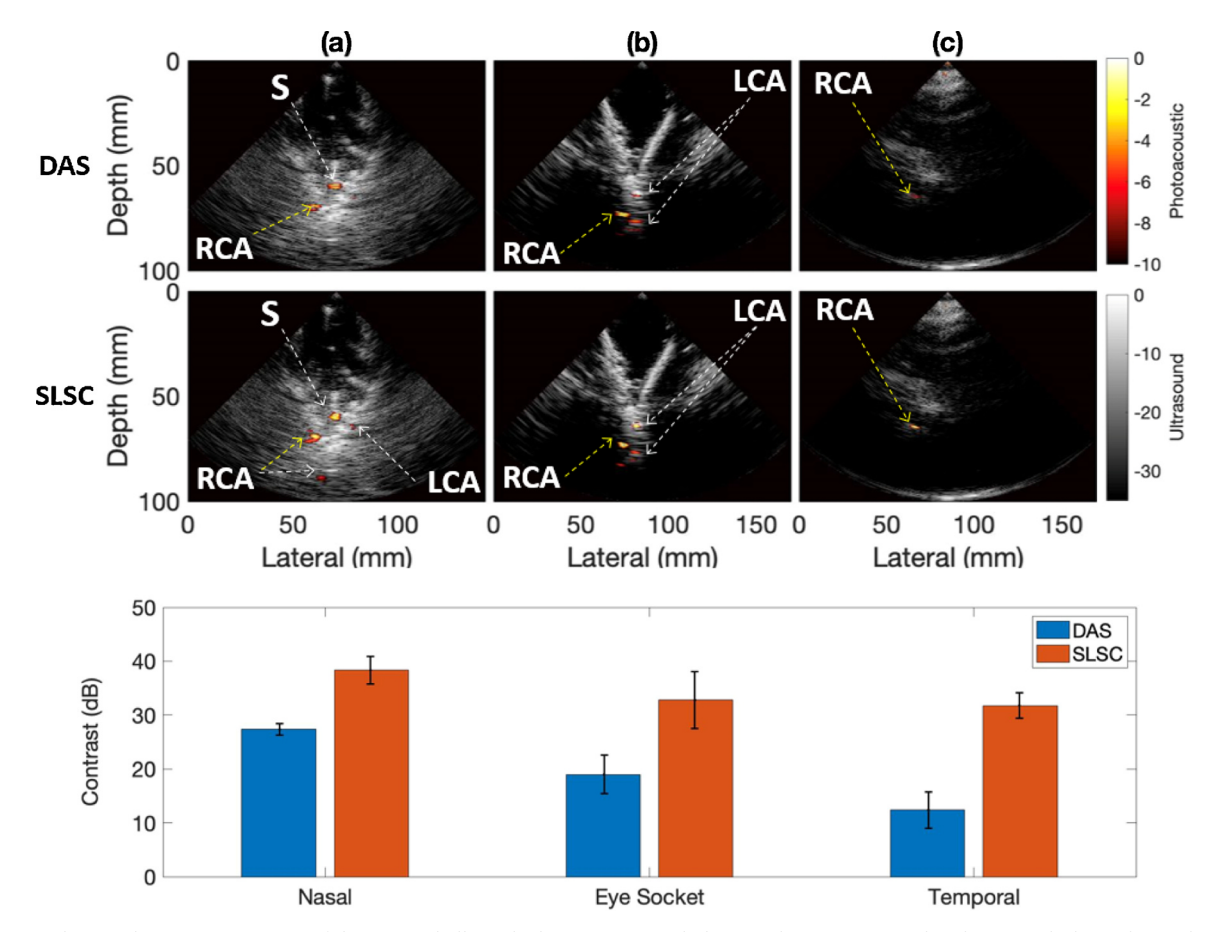


Fig. 11. DAS and SLSC photoacoustic images of the empty skull overlaid on co-registered ultrasound images acquired with (a) nasal, (b) ocular, and (c) temporal probe locations. The optical source (S) emitted 3, 5, and 4 mJ per pulse, respectively. Each photoacoustic image was normalized to its brightest pixel and displayed with 10 dB dynamic range. The sphenoid and temporal bone thicknesses were 0 mm and 1 mm, respectively. The RCA signal labeled with the yellow arrow was used to compute contrast.

contrast (Fig. 12(b)). When imaging from the right eye, the RCA was visualized with 18 dB and 33 dB contrast in DAS and SLSC images, respectively (Figs. 12(c) and 12(d), respectively). Fig. 12(e) shows the photoacoustic-to-CT registration for the the RCA, visualized with the photoacoustic receiver located on the right cadaver eye. The

photoacoustic signals originate from the same location as the RCA, which confirms visualization of the RCA.

Fig. 13 compares the contrast of photoacoustic DAS and SLSC images of the ICAs when the tight source was placed on the ICA of interest and viewed from the ocular region on the same side as the ICA.

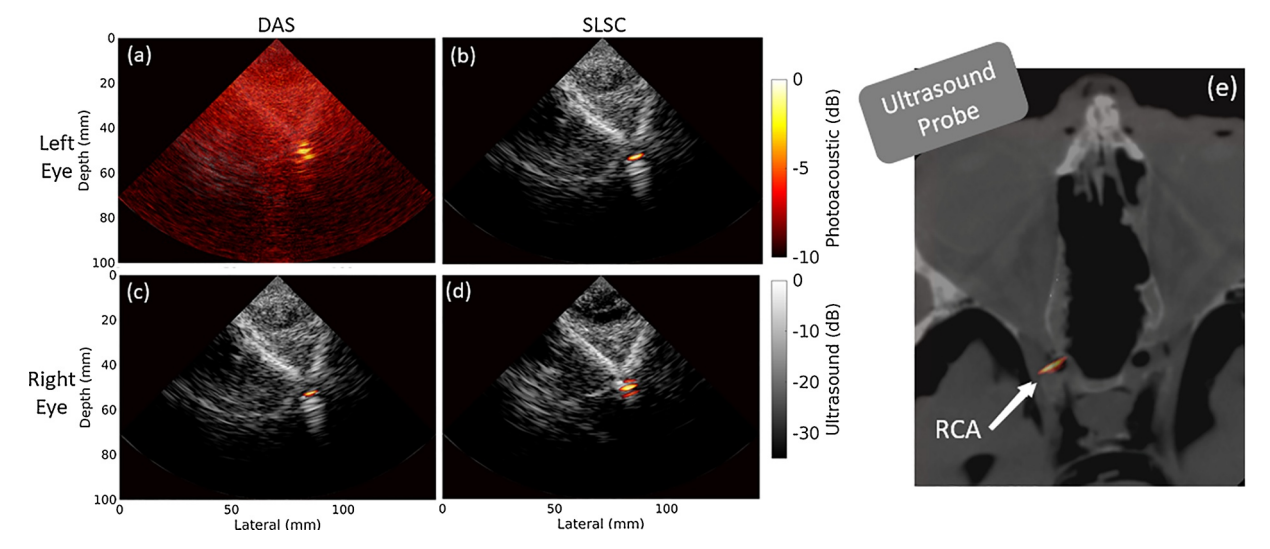
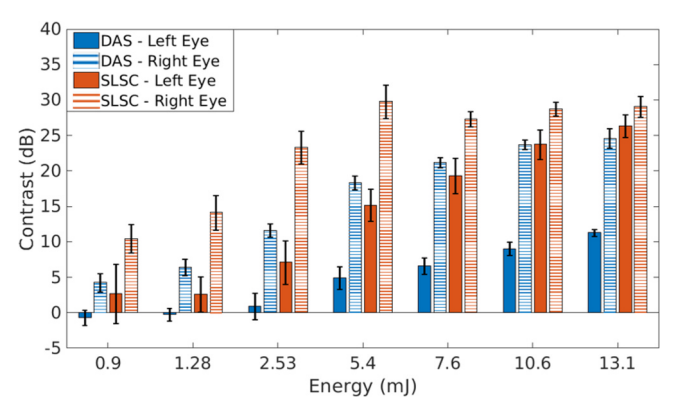


Fig. 12. (a,c) DAS and (b,d) SLSC photoacoustic images from the fresh cadaver, overlaid on co-registered ultrasound images acquired with (a,b) left and (c,d) right ocular probe locations. The light source operated at 5.4 mJ per pulse and was placed on the LCA (visualized through the left eye) or RCA (visualized through the right eye). (e) Co-registered CT (gray scale) and photoacoustic image (color) images acquired with the ultrasound probe placed on the right eyelid of the cadaver head.



**Fig. 13.** Contrast of the ICAs in DAS and SLSC photoacoustic images from the fresh cadaver head when the ultrasound probe was located on the left or right eye (as indicated in the legend), and the light source illuminated the ICA located on the same side as the probe.

For this setup, the measured contrasts in DAS images obtained from the right ocular region were 5.0 - 14.7 dB greater than those obtained from the left ocular region. Therefore, the right eye was determined to be the preferable location for DAS photoacoustic imaging of the ICAs in this cadaver head. This result also shows that SLSC imaging raised target contrasts and reduced the contrast difference between images obtained from the left and right eyes, when compared the differences observed with DAS imaging. For example, at energy levels 10.6 and 13.1 mJ per pulse, the SLSC images from the left and right eye experienced a 2 - 5 dB difference in contrast values with SLSC imaging (compared to 13 - 15 dB with DAS imaging). Therefore, SLSC beamforming can be used to reduce left-right asymmetries in the contrast of amplitude-based DAS photoacoustic images, which are likely caused by asymmetrical bone structures.

Fig. 14 shows the minimum energy required to visualize the ICAs with at least 5 dB contrast at two different optical source-to-target distances (i.e., 0 and 1.5 cm). The 1.5 cm distance represents imaging capabilities when the ICA is difficult to locate during surgery. In both cases, SLSC imaging reduces the minimum required energy for ICA visualization compared to DAS imaging by 0.4 - 5.1 mJ and 3.9 - 5.5 mJ for the source-to-target distances of 0 cm and 1.5 cm, respectively. Although the LCA was not visualized with DAS imaging within safety limits when the source-to-target distance was 1.5 cm, SLSC imaging successfully visualized this target within safety limits.

Fig. 15 reports contrast as a function of multiple source-to-target distances for DAS and SLSC imaging. When the light source was placed

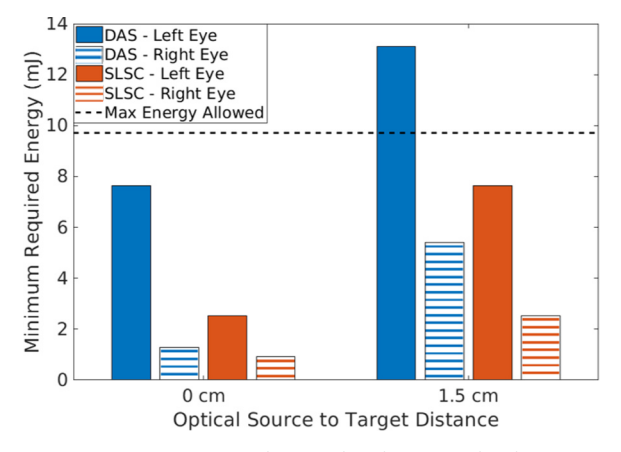


**Fig. 14.** Minimum energy required to visualize the ICAs with 5 dB contrast with DAS and SLSC imaging when the optical source was placed at stationary distances of 0 cm and 1.5 cm away from the ICA target located on the same side as the probe (which is indicated in the legend).

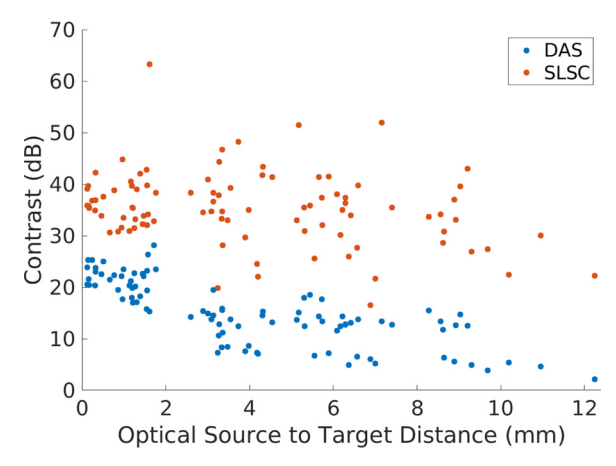


Fig. 15. DAS contrast measurements from photoacoustic images of the right ocular region as the light source was navigated in the sphenoid sinus of the fresh cadaver head and the distance between the light source and RCA was increased.

on the RCA target (i.e., 0 mm distance), this target was visualized with 20 - 25 dB contrast with DAS imaging, with lower contrast observed at larger distances. When the light source was translated up to 9 mm away from the target, the RCA was visualized with 5 - 15 dB contrast with DAS imaging. At distances > 9 mm, contrast drops below the 5 dB threshold with DAS imaging, while SLSC imaging continues to provide superior contrast at multiple source-to-target distances.

## 4. Discussion

This work investigated the propagation of acoustic waves within human cadaveric skull specimens in simulation and experimental studies in order to determine the optimal ultrasound probe locations for photoacoustic imaging during minimally invasive surgeries of the skull base. The complex bony anatomy of the human skull significantly impacts the propagation of acoustic waves from internal photoacoustic sources to external acoustic receivers placed on the skull during a surgical procedure, as indicated by k-Wave simulations (Fig. 6). Concave bony surfaces trap acoustic signal in the frontal cranium which causes reverberations and increases the length of the acoustic pathway from source to sensor. Therefore, higher energy optical sources, advanced beamforming techniques, and strategic placement of the ultrasound probe are necessary to generate high contrast and interpretable transcranial photoacoustic images.

Although the temporal region was previously proposed as a possible location for ultrasound probe placement [14–17], this location performed more poorly when considering both simulation and experimental results (see Figs. 7 and 10(a,b), respectively). Specifically, when the temporal bone was thicker than 1.3 mm, it was not possible for the targets to be seen within energy safety limits. Considering that the adult human temporal bone measures 1 - 4.4 mm [54], the temporal bone is generally not a feasible location for placing the ultrasound probe in light of these results, likely due to the trapping, reverberation, and attenuation of the acoustic signals observed in Figs. 6 and 7(b).

Both k-Wave simulations and empty skull experimental results agree that placing the ultrasound probe in the nasal cavity would receive the highest photoacoustic pressure and therefore produce the highest contrast photoacoustic images (Figs. 7 and 11). The nasal cavity also enabled simultaneous visualization of the LCA, RCA, and optical source. Simultaneous visualization of these three sources is advantageous to determine the proximity of the surgical tool to the ICAs when the optical source can be attached the thool tip [14,36] or when visualization of endonasal tool tips is otherwise needed. In addition, the corresponding nasal cavity ultrasound image has the potential to provide an intuitive imaging plane for surgeons.

Despite these benefits, placing the probe in the nasal cavity has three logistical barriers. First, a forward-looking endoscopic ultrasound probe is required. Second, space constraints limit the use of endoscopic probes in conjunction with light delivery systems and other surgical tools. Third, as the probe is inserted into the nasal cavity, an acoustic coupling medium such as water or gel would be required in the naturally air-filled pathway [55]. One potential solution to provide acoustic coupling is to attach a water-filled balloon to a re-designed nasal ultrasound probe, as previously implemented for ultrasound endoscopy procedures [56–58]. Similar innovations could be implemented to address the remaining barriers. From this perspective, the work presented in this paper regarding nasal probe locations both demonstrates the need for novel photoacoustic and ultrasonic nasal probes and takes an additional step to outline preliminary design and energy requirements for these probes.

The ocular region was the second most optimal position based on the magnitude of the photoacoustic signal received in simulations and photoacoustic experiments (see Figs. 7 and 11), but we consider it to be the most optimal from a logistics perspective for the following two reasons. First, this position can be used with standard ultrasound probes and acoustic coupling gel and therefore can be more readily integrated in the surgical suite. Second, the absence of the ultrasound probe in the nasal cavity maintains sufficient space for the light delivery method, which is a critical component of the proposed photoacoustic imaging solution in cases where the ICAs cannot be located by endoscopy alone. To demonstrate additional feasibility of the ocular ultrasound probe position, we created a setting in the cadaver head experiments mimicking a case where the surgeon would move the light source around the sphenoid sinus in search of the photoacoustic ICA signal (see Fig. 15). Results demonstrate visualization of the RCA with DAS and SLSC beamforming when the optical source-to-RCA distance was  $\leq 9$ mm, which is well within the bounds of the average 2 cm diameter surgical site [11]. To improve maneuverability, we designed a light delivery system with a small form factor (see Table 1 and Fig. 4) to better fit the confined space of the nasal cavity while meeting the requirements of emitting sufficient energy and remaining within safety limits. This design has the potential to be improved in the future through incorporation of diffusers at the fiber bundle tip to reduce the device size, increase the beam divergence angle, and shorten the quartz spacer length.

There are three limitations introduced with the ocular probe reception of the photoacoustic signals produced by this new light delivery design. First, the optical source is outside of the imaging plane, which can possibly be addressed by relying on the DAS contrast measurements to assess the source-to-target distance. Second, only one ICA will likely be present in the imaging plane at any given time (rather than both ICAs), as seen in the cadaver head experiment. Third, the ICA on the same side as the ocular region is likely to be visualized over the ICA on the opposite side (e.g., LCA when visualizing signals though the left ocular region). Although the RCA was visualized from the left ocular region in the filled skull experiment, it was not visible from the left ocular region in the cadaver head experiment. We suspect that the source of this discrepancy was the difference in acoustic coupling. Specifically, the water in the filled skull likely provided acoustic coupling for the acoustic waves traveling from the RCA, across the nasal cavity, to the probe on the left eye, while the air naturally contained within this acoustic pathway in the fresh cadaver head prevented acoustic coupling. The second and third limitations can possibly be addressed by simultaneously placing a novel ultrasound probe design on each eye.

Many of our observations about SLSC beamforming are consistent with previously reported advantages and disadvantages of this coherence-based beamformer [14,17,32–34]. For example, SLSC imaging is advantageous over DAS when the goal is to produce high contrast photoacoustic images of the ICAs in the presence of low laser fluence and attenuating tissues such as bone (Figs. 11, 12, 13). However,

because coherence-based imaging is less sensitive to changes in fluence, an amplitude-based beamformer such as DAS is more promising when the goal is to use image contrast to estimate source-to-target distances (Fig. 15). The results in Fig. 10(b) additionally demonstrate that SLSC images generally reduced the required energy to visualize the ICA targets when compared to requirements with DAS images.

One additional significant outcome of the studies presented in this paper is that they indicate the promise of the simulation methodology for patient-specific preoperative surgical planning of optimal receiver locations when using photoacoustic imaging as an intraoperative navigation technique. Variations in skull anatomy between individuals as well as asymmetry in skull anatomy within an individual alters the characteristics of the acoustic pathway from the ICA photoacoustic source to the externally placed acoustic receivers. We demonstrated that skull anatomy asymmetry within an individual has a potential effect on photoacoustic image quality. It is therefore probable that in extreme cases of asymmetry, one of the ocular regions may be eliminated as a feasible probe location. Conversely, it is also possible that in extreme cases of inter-patient variability, more feasible probe locations would be available.

#### 5. Conclusion

The work presented in this paper details significant requirements for progression toward patient studies of transcranial intraoperative photoacoustic imaging of the internal carotid arteries. The nasal cavity and ocular regions were identified as feasible locations for the ultrasound probe. We then designed a custom light delivery method and demonstrated its use in a fresh cadaver head. In addition, we demonstrated that photoacoustic k-Wave simulations can potentially be used with preoperative CT scans as a patient-specific surgical planning tool to choose the most optimal probe position. Advanced beamforming techniques, such as SLSC, are preferable over DAS when the goal is to produce high contrast photoacoustic images of the ICAs during minimally invasive neurosurgeries. DAS is more promising when the goal is to use image contrast to estimate source-to-target distances. A single optical wavelength was used for these demonstrations, while future wavelength optimization has the potential to preferentially excite oxyghemoglobin in the ICAs over deoxyhemoglobin in the venous plexus surrounding the surgical site. Overall, this translational research demonstrates that photoacoustic imaging is a promising technique for guidance of endonasal transsphenoidal surgeries.

#### **Conflict of Interest**

The authors declare that there are no conflicts of interest.

## Acknowledgments

This research was financially supported by NIH Grant No. R00-EB018994, NSF CAREER Award Grant No. ECCS 1751522, and the NSF Graduate Research Fellowship Program (Grant No. DGE1746891). The authors thank Peter Kazanzides for sharing the Mayfield clamp used in these studies and Mohammed Lehar for assistance with preparing the bone fragment samples. The study sponsors had no involvement with the study design, the data collection, analysis, and interpretation, the writing of research reports, nor the decision to submit this article for publication.

#### References

- [1] R.J. Komotar, R.M. Starke, D.M. Raper, V.K. Anand, T.H. Schwartz, Endoscopic endonasal compared with microscopic transsphenoidal and open transcranial resection of giant pituitary adenomas, Pituitary 15 (2) (2012) 150–159.
- [2] M. Buchfelder, J. Kreutzer, Transcranial surgery for pituitary adenomas, Pituitary 11 (4) (2008) 375–384.
- [3] P.F. Svider, M.J. Pines, M.D. Raikundalia, A.J. Folbe, S. Baredes, J.K. Liu, J.A. Eloy,

- Transsphenoidal surgery for malignant pituitary lesions: an analysis of inpatient complications, International forum of allergy & rhinology, Vol. 5 (2015) 659–664.
- [4] P. Cappabianca, L.M. Cavallo, E. de Divitiis, Endoscopic endonasal transsphenoidal surgery, Neurosurgery 55 (2004) 933–941.
- [5] X. Zhang, Z. Fei, W. Zhang, J. Zhang, W. Liu, L. Fu, W. Cao, S. Jiang, X.F. Song, Endoscopic endonasal transsphenoidal surgery for invasive pituitary adenoma, Journal of Clinical Neuroscience 15 (2008) 241–245.
- [6] I. Ciric, A. Ragin, C. Baumgartner, D. Pierce, Complications of transsphenoidal surgery: Results of a national survey, review of the literature, and personal experience, Neurosurgery 40 (2) (1997) 225–237.
- [7] M.S. Agam, M.A. Wedemeyer, B. Wrobel, M.H. Weiss, J.D. Carmichael, G. Zada, Complications associated with microscopic and endoscopic transsphenoidal pituitary surgery: experience of 1153 consecutive cases treated at a single tertiary care pituitary center, Journal of Neurosurgery JNS 130 (5) (2018) 1576–1583.
- [8] M.O. Perry, W.H. Snyder, E.R. Thal, Carotid artery injuries caused by blunt trauma, Annals of Surgery 192 (1) (1980) 74–77.
- [9] J. Raymond, J. Hardy, R. Czepko, D. Roy, Arterial injuries in transsphenoidal surgery for pituitary adenoma; the role of angiography and endovascular treatment, American Journal of Neuroradiology 18 (4) (1997) 655–665.
- [10] L.C. Heringer, M.F. de Oliveira, J.M. Rotta, R.V. Botelho, Effect of repeated transsphenoidal surgery in recurrent or residual pituitary adenomas: A systematic review and meta-analysis, Surgical Neurology International 7 (2016) 1–6.
- [11] M.A. Mascarella, R. Forghani, S.D. Maio, D. Sirhan, A. Zeitouni, G. Mohr, M.A. Tewfik, Indicators of a reduced intercarotid artery distance in patients undergoing endoscopic transsphenoidal surgery, Journal of Neurological Surgery, Part B Skull Base 76 (3) (2015) 195–201.
- [12] K. Kitazawa, H. Okudera, T. Takemae, S. Kobayashi, CT guided transsphenoidal surgery: report of nine cases, Neurological Surgery 21 (147) (1993).
- [13] X. Wang, D.L. Chamberland, G. Xi, Noninvasive reflection mode photoacoustic imaging through infant skull toward imaging of neonatal brains, Journal of Neuroscience Methods 168 (2) (2008) 412–421.
- [14] M.A.L. Bell, A.K. Ostrowski, K. Li, P. Kazanzides, E.M. Boctor, Localization of transcranial targets for photoacoustic-guided endonasal surgeries, Photoacoustics 3 (2) (2015) 78–87.
- [15] M.A.L. Bell, A.K. Ostrowski, P.K. Ke Li, E. Boctor, Quantifying bone thickness, light transmission, and contrast interrelationships in transcranial photoacoustic imaging, SPIE BiOS 9323 (2015).
- [16] M.A.L. Bell, A.B. Dagle, P. Kazanzides, E.M. Boctor, Experimental assessment of energy requirements and tool tip visibility for photoacoustic-guided endonasal surgery. SPIE BiOS (2016).
- [17] M.A.L. Bell, A.K. Ostrowski, P. Kazanzides, E.M. Boctor, Feasibility of transcranial photoacoustic imaging for interventional guidance of endonasal surgeries, SPIE BiOS 8943 (2014).
- [18] T. Kirchner, J. Gröhl, N. Holzwarth, M.A. Herrera, A. Hernández-Aguilera, E. Santos, L. Maier-Hein, Photoacoustic monitoring of blood oxygenation during neurosurgical interventions, in: A.A. Oraevsky, L.V. Wang (Eds.), Photons Plus Ultrasound: Imaging and Sensing 2019, Vol. 10878, International Society for Optics and Photonics, SPIE, 2019, pp. 14–18.
- [19] M.F. Kircher, A. De La Zerda, J.V. Jokerst, C.L. Zavaleta, P.J. Kempen, E. Mittra, K. Pitter, R. Huang, C. Campos, F. Habte, et al., A brain tumor molecular imaging strategy using a new triple-modality mri-photoacoustic-raman nanoparticle, Nature Medicine 18 (5) (2012) 829.
- [20] P. Beard, Biomedical photoacoustics, Interface Focus 1 (4) (2011) 602–631, https://doi.org/10.1098/rsfs.2011.0028.
- [21] J. Yu, H. Nguyen, W. Steenbergen, K. Kim, Recent development of technology and application of photoacoustic molecular imaging toward clinical translation, Journal of Nuclear Medicine 59 (8) (2018) 1202–1207.
- [22] M. Kneipp, J. Turner, H. Estrada, J. Rebling, S. Shoham, D. Razansky, Effects of the murine skull in optoacoustic brain microscopy, Journal of Biophotonics 9 (1-2) (2016) 117–123.
- [23] G. Pinton, J.-F. Aubry, E. Bossy, M. Muller, M. Pernot, M. Tanter, Attenuation, scattering, and absorption of ultrasound in the skull bone, Medical Physics 39 (1) (2012) 299–307.
- [24] H. Estrada, J. Rebling, J. Turner, D. Razansky, Broadband acoustic properties of a murine skull, Physics in Medicine & Biology 61 (5) (2016) 1932.
- [25] S. Golovynskyi, I. Golovynska, L.I. Stepanova, O.I. Datsenko, L. Liu, J. Qu, T.Y. Ohulchanskyy, Optical windows for head tissues in near-infrared and shortwave infrared regions: Approaching transcranial light applications, Journal of Biophotonics 11 (12) (2018) e201800141.
- [26] L. Nie, X. Cai, K.I. Maslov, A. Garcia-Uribe, M.A. Anastasio, L.V. Wang, Photoacoustic tomography through a whole adult human skull with a photon recycler, Journal of Biomedical Optics 17 (11) (2012) 110506.
- [27] Q. Xu, B. Volinski, A. Hariri, A. Fatima, M. Nasiriavanaki, Effect of small and large animal skull bone on photoacoustic signal, in: Photons Plus Ultrasound: Imaging and Sensing 2017, 10064, International Society for Optics and Photonics, 2017, p. 100643S.
- [28] H. Estrada, X. Huang, J. Rebling, M. Zwack, S. Gottschalk, D. Razansky, Virtual craniotomy for high-resolution optoacoustic brain microscopy, Scientific Reports 8 (1) (2018) 1459.
- [29] S. Govinahalli Sathyanarayana, B. Ning, R. Cao, S. Hu, J.A. Hossack, Dictionary learning-based reverberation removal enables depth-resolved photoacoustic microscopy of cortical microvasculature in the mouse brain, Scientific Reports 8 (1) (2018) 985.
- [30] C. Huang, L. Nie, R.W. Schoonover, Z. Guo, C.O. Schirra, M.A. Anastasio, L.V. Wang, Aberration correction for transcranial photoacoustic tomography of primates employing adjunct image data, Journal of Biomedical Optics 17 (6) (2012)

066016.

- [31] S. Purkayastha, F. Sorond, Transcranial doppler ultrasound: Technique and application, Semin Neurol 32 (04) (2012) 411–420.
- [32] M.A.L. Bell, N. Ku, D.Y. Song, E.M. Boctor, Short-lag spatial coherence beamforming of photoacoustic images for enhanced visualization of prostate brachytherapy seeds, Biomedical Optics Express 4 (10) (2013) 1964.
- [33] M.A.L. Bell, N.P. Kuo, D.Y. Song, J.U. Kang, E.M. Boctor, In vivo visualization of prostate brachytherapy seeds with photoacoustic imaging, Journal of Biomedical Optics 19 (12) (2014) 126011.
- [34] M.A.L. Bell, X. Guo, D.Y. Song, E.M. Boctor, Transurethral light delivery for prostate photoacoustic imaging, Journal of Biomedical Optics 20 (3) (2015) 036002.
- [35] S. Kim, Y. Tan, P. Kazanzides, M.A.L. Bell, Feasibility of photoacoustic image guidance for telerobotic endonasal transsphenoidal surgery, IEEE International Conference on Biomedical Robotics and Biomechatronics (BioRob) 6 (2016).
- [36] B. Eddins, M.A.L. Bell, Design of a multifiber light delivery system for photoacoustic-guided surgery, Biomedical Optics Express 22 (2017).
- [37] B.E. Treeby, B.T. Cox, k-Wave: MATLAB toolbox for the simulation and reconstruction of photoacoustic wave fields, Journal of Biomedical Optics 15 (2) (2010) 1-12-12
- [38] B.E. Treeby, B.T. Cox, J. Jaros, A MATLAB Toolbox for the Time Domain Simulation of Acoustic Wave Fields User Manual, (2016) Manual Version: 1.1.
- [39] M. Tabei, T.D. Mast, R. Waag, A k-space method for coupled first-order acoustic propagation equations, The Journal of the Acoustical Society of America 111 (1) (2002) 53-63
- [40] N. Ugryumova, S.J. Matcher, D.P. Attenburrow, Measurement of bone mineral density via light scattering, Physics in Medicine & Biology 49 (3) (2004) 469.
- [41] P. Van der Zee, M. Essenpreis, D.T. Delpy, Optical properties of brain tissue, in: Photon Migration and Imaging in Random Media and Tissues, Vol. 1888, International Society for Optics and Photonics, 1993, pp. 454–465.
- [42] S.K.V. Sekar, I. Bargigia, A. Dalla Mora, P. Taroni, A. Ruggeri, A. Tosi, A. Pifferi, A. Farina, Diffuse optical characterization of collagen absorption from 500 to 1700 nm, Journal of Biomedical Optics 22 (1) (2017) 015006.
- [43] R.L. van Veen, H. Sterenborg, A. Pifferi, A. Torricelli, R. Cubeddu, Determination of VIS-NIR absorption coefficients of mammalian fat, with time-and spatially resolved diffuse reflectance and transmission spectroscopy, Biomedical Topical Meeting, OSA Technical Digest (Optical Society of America), 2004 pSF4.
- [44] D.J. Segelstein, The complex refractive index of water, Ph.D. thesis, University of Missouri-Kansas City, 1981.
- [45] S. Praul, Tabulated molar extinction coefficient for hemoglobin in water, https://omlc.org/spectra/hemoglobin/summary.html, accessed: 2020-03-18.
- [46] S.L. Jacques, R.D. Glickman, J.A. Schwartz, Internal absorption coefficient and threshold for pulsed laser disruption of melanosomes isolated from retinal pigment epithelium, Laser-Tissue Interaction VII, Vol. 2681 (1996) 468–477.
- [47] S.L. Jacques, D.J. McAuliffe, The melanosome: threshold temperature for explosive vaporization and internal absorption coefficient during pulsed laser irradiation, Photochemistry and Photobiology 53 (6) (1991) 769–775.
- [48] J.L. Su, R.R. Bouchard, A.B. Karpiouk, J.D. Hazle, S.Y. Emelianov, Photoacoustic imaging of prostate brachytherapy seeds, Biomedical Optics Express 2 (8) (2011) 2243–2254.
- $\mbox{ [49]}$  American National Standards Institute, American national standard for the safe use of lasers, (2007).
- [50] S. Ley, M. Stadthalter, D. Link, D. Laqua, P. Husar, Phantom materials mimicking the optical properties in the near infrared range for non-invasive fetal pulse oximetry, 2014 36th Annual International Conference of the IEEE Engineering in Medicine and Biology Society, 2014, EMBC, 2014, pp. 1432–1435.
- [51] A.I. Chen, M.L. Balter, M.I. Chen, D. Gross, S.K. Alam, T.J. Maguire, M.L. Yarmush, Multilayered tissue mimicking skin and vessel phantoms with tunable mechanical, optical, and acoustic properties, Medical Physics 43 (6) (2016) 3117–3131.
- [52] S.A. Filatova, I.A. Shcherbakov, V.B. Tsvetkov, Optical properties of animal tissues in the wavelength range from 350 to 2600 nm, Journal of Biomedical Optics 22 (3) (2017) 035009.
- [53] M.A.L. Bell, G.E. Trahey, B.C. Byran, J.J. Dahl, Short-lag spatial coherence of backscattered echoes: imaging characteristics, IEEE Transactions on Ultrasonics, Ferroelectrics, and Frequency Control 58 (7) (2011) 1377–1388.
- [54] S. Ma, L.J. Baillie, M.D. Stringer, Reappraising the surface anatomy of the pterion and its relationship to the middle meningeal artery, Clinical Anatomy 25 (3) (2012) 330–339.
- [55] S. Yoshinaga, I. Oda, S. Nonaka, R. Kushima, Y. Saito, Endoscopic ultrasound using ultrasound probes for the diagnosis of early esophageal and gastric cancers, World J Gastrointest Endosc 4 (6) (2012) 218–226.
- [56] A. Chung, V. Kwan, Endoscopic ultrasound: an overview of its role in current clinical practice, Australasian Journal of Ultrasound in Medicine 12 (2) (2009) 21–29.
- [57] H. Inoue, T. Kawano, K. Takeshita, T. Iwai, Modified soft-balloon methods during ultrasonic probe examination for superficial esophageal cancer, Endoscopy 30(S1 (1998) A-41.
- [58] M.B. Wallace, B.J. Hoffman, A.S. Sahai, H. Inoue, A. Van Velse, R.H. Hawes, Imaging of esophageal tumors with a water-filled condom and a catheter US probe, Gastrointestinal Endoscopy 51 (5) (2000) 597–600.



Michelle T. Graham is a graduate student in the Department of Electrical and Computer Engineering at Johns Hopkins University. She received her B.S. degree in biophysics (engineering minor) from the University of Scranton in 2015 and her M.S.E degree in electrical and computer engineering from Johns Hopkins University in 2018. Her research interests include intraoperative photoacoustic imaging, neurosurgical guidance, and translational research. She is a recipient of the NSF Graduate Research Fellowship.



Jiaqi Huang is a graduate student in the Department of Biomedical Engineering at Johns Hopkins University, pursing the M.S.E. degree with a focus on imaging and instrumentation. She received her B.S. degree in Engineering Science - Biomedical Systems from the University of Toronto in 2018.



Francis Creighton is an Assistant Professor of Otolaryngology at Johns Hopkins University School of Medicine. He is a neurotologist and lateral skull base surgeon specializing in surgical and medical treatment of the middle ear, inner ear, skull base, and facial nerve disorders. He received his medical degree from Emory University School of Medicine in 2012. He completed a residency in Otolaryngology at the Massachusetts Eye and Ear Infirmary in 2017, followed by a head and neck surgery/otolaryngology fellowship at Johns Hopkins University School of Medicine in 2019. His research focuses on the integration of mobotic and augmented reality platforms to improve surgical safety and efficiency



Muyinatu A. Lediju Bell is an Assistant Professor of Electrical and Computer Engineering, Biomedical Engineering, and Computer Science at Johns Hopkins University, where she founded and directs the Photoacoustic & Ultrasonic Systems Engineering (PULSE) Lab. She received her Ph.D. in biomedical engineering from Duke University in 2012, completed research abroad as a Whitaker International Fellow in 2010, and earned her B.S. degree in mechanical engineering (biomedical engineering minor) from Massachusetts Institute of Technology in 2006. Her research interests include ultrasound and photoacoustic imaging, photoacoustic-guided surgery, robot-assisted imaging, beamforming, medical device design, and clinical

translation of novel medical imaging technologies that will improve the standard of cancer patient care. She is a recipient of multiple awards and honors, including MIT Technology Review's Innovator Under 35 Award (2016), the NSF CAREER Award (2018), the NIH Trailblazer Award (2018), the Alfred P. Sloan Research Fellowship (2019), the ORAU Ralph E. Powe Jr. Faculty Enhancement Award (2019), and Maryland's Outstanding Young Engineer Award (2019). Dr. Bell currently serves on the Editorial Board of *Photoacoustics*.